

ARTICLES

Measurement of the reaction ${}^3\text{He}(\gamma, pp)n$ and its relation to three-body forcesA. J. Sarty, K. G. R. Doss,* G. Feldman, E. L. Hallin, R. E. Pywell, G. A. Retzlaff,
D. M. Skopik, and H. R. Weller†*Saskatchewan Accelerator Laboratory, University of Saskatchewan, Saskatoon, Saskatchewan, Canada S7N 0W0*

W. R. Dodge,‡ J. W. Lightbody Jr.,§ and J. S. O'Connell**

National Institute of Standards and Technology, Gaithersburg, Maryland 20899

C. C. Chang

Department of Physics, University of Maryland, College Park, Maryland 20742

(Received 28 August 1992)

The three-body photodisintegration of ${}^3\text{He}$ has been measured at photon energies ranging from 90 to 250 MeV, in kinematic regions where three-body forces effects are expected to be maximized, and two-body mechanisms suppressed. The differential cross sections as a function of neutron momentum demonstrate that calculations using only one-body and two-body photoabsorption mechanisms cannot describe the data and that a two-pion-exchange, three-body absorption mechanism is needed to adequately describe the data.

PACS number(s): 25.20.Dc, 25.10.+s, 21.30.+y

I. INTRODUCTION

Evidence for the existence of three-body forces in nuclei lies mainly in the explanation of binding energies in the trinucleon systems, ${}^3\text{He}$ and ${}^3\text{H}$. However, the evidence is indirect and not completely satisfactory, since the "exact" Faddeev binding energy predictions which include a two-pion exchange term (2π - $3N$) all lead to overbinding [1]. More recent photodisintegration measurements [2,3] of the three-body breakup of ${}^3\text{He}$ have focused upon restricting the available three-body phase space to select regions sensitive to 2π - $3N$ components, while reactions such as (π, NN) have attempted to look for enhancements over the dominant $2N$ pion absorption mechanisms [4].

Earlier experiments [5] have confirmed that three-body photodisintegration in ${}^3\text{He}$ is dominated by $2N$ absorption on a correlated np pair. Therefore, to study $3N$ absorption, we need to move to a region of three-body phase space that is not overwhelmed by these $2N$ mechanisms. Laget has pointed out that a kinematic situation

corresponding to the photon interacting with a diproton has the desirable effect of minimizing $2N$ contributions and emphasizing effects due to the $3N$ force [6], for these reasons: (1) The pp pair has no dipole moment to which the photon can couple. (2) The formation of the Δ as an intermediate state is forbidden by spin-isospin considerations. (3) Charged meson exchange currents vanish.

II. THEORY

The only published calculations of the ${}^3\text{He}(\gamma, pp)n$ reaction specifically aimed at estimating $3N$ absorption mechanisms are those by Laget [6,7] in which the measured laboratory differential cross section is related by a Jacobian to what is termed a "reduced cross section" as

$$\frac{d^3\sigma_{\text{lab}}}{dp_1 d\Omega_1 d\Omega_2} = \frac{E_n p_1^2}{E_1 |E_n p_2^2 - E_2 \mathbf{p}_n \cdot \mathbf{p}_2|} \left[\frac{W_{pp}}{p_1} \right]_{\text{c.m.}} \times \frac{d^3\sigma_{\text{red}}}{(d\Omega_1)_{\text{c.m.}} d\Omega_n dp_n}, \quad (1)$$

where (E_1, \mathbf{p}_1) , (E_2, \mathbf{p}_2) , and (E_n, \mathbf{p}_n) are the four-momenta of the outgoing two protons and the neutron. The quantities $[p_1]_{\text{c.m.}}$ and W_{pp} are the proton momentum and total energy of the two detected protons measured in their c.m. frame, where the proton labeled "1" is defined as the proton emitted on the side of the beam opposite to the neutron. The identification of proton "1" is only meaningful for coplanar kinematics in which the two protons are on opposing sides of the incident photon beam. This reduced cross section is essentially the product of the neutron momentum distribution and the cross section for the disintegration of a pp pair [8] when the

*Permanent address: Regina General Hospital, Nuclear Medicine Dept., Regina, Saskatchewan, Canada S4P 0W5.

†Permanent address: Triangle Universities Nuclear Laboratory, Duke University, Durham, NC 27706.

‡Permanent address: Department of Physics, George Washington University, Washington, DC 20052.

§Permanent address: Division of Physics, National Science Foundation, 1800 G Street N.W., Washington, D.C. 20550.

**Permanent address: Booz, Allen & Hamilton Inc., Crystal Square 2, Suite 1100, 1725 Jefferson Davis Highway, Arlington, Virginia 22202-4163.

neutron is assumed to be a spectator moving in a relative S state with respect to the active pp pair. Note that we have slightly changed the notation used in Ref. [6] to reflect the actual number of cross section differentials on each side of the equation.

Laget's calculations are done using the diagrammatic expansions shown in Fig. 1. In these diagrams, the open circles represent full transition amplitudes [8] (T matrices) and the filled circles are just the γNN and πNN vertices. The $3N$ absorption mechanism shown in diagram 1g represents the primary $3N$ process for the ${}^3\text{He}(\gamma, pp)n$ reaction. Above the energy for which pions are kinematically allowed [6] the calculation is basically free of parameters. The calculated $3N$ absorption cross section contains a logarithmic singularity associated with the on-shell propagation of the "first" exchanged pion, thus the choice of kinematics can enhance the contributions of such $3N$ mechanisms. Below the kinematic threshold for pions, both exchanged mesons are off their mass shell and these three-body exchange currents can be linked by gauge invariance to the corresponding three-body forces [6,9]. The numerical difficulty of integrating over the logarithmic singularity is avoided for this kinematic case but the calculation is now dependent upon off-shell extrapolations [6].

The enhancement in the ${}^3\text{He}(\gamma, pp)n$ cross section due to the inclusion of the $3N$ diagrams is maximized when the neutron is emitted with $\theta_n^{\text{lab}} = 45^\circ$ and $p_n^{\text{lab}} \cong 300$ MeV/c. This corresponds to the most likely kinematics of the recoil nucleon in pion photoproduction on a nucleon at rest [6]. An additional enhancement of the relative contribution of the $3N$ diagrams can be achieved by choosing the proton angle $[\theta_1]_{\text{c.m.}}$ to correspond to 90° with respect to (w.r.t.) the direction of the incoming photon in order to minimize $E2$ absorption. The angle $[\theta_1]_{\text{c.m.}}$ is the angle of proton-1, measured in the pp -center of mass system w.r.t. the direction of the incident photon in the laboratory.

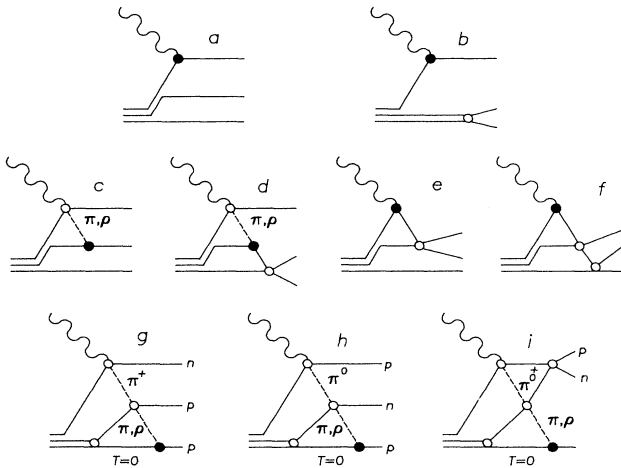


FIG. 1. Diagrams for ${}^3\text{He}(\gamma, pp)n$ used by Laget. (a) The $1N$ absorption mechanism, and (b) $1N + \text{FSI}$. (c) and (e) $2N$ absorption, and (d) and (f) $2N + \text{FSI}$. (g) and (h) $3N$ mechanisms, and (i) $3N + \text{FSI}$.

Reduced cross sections, for three different energies, are shown in Fig. 2. The dash-dotted curves (labeled $2N_{\text{DW}}$) include all $1N$ (diagram 1a), $1N + \text{FSI}$ (final state interactions) (diagram 1b), $2N$ (diagrams 1c and 1e), and $2N + \text{FSI}$ (diagrams 1d and 1f) mechanisms. The dashed curves ($3N_{\text{PW}}$) include the $3N$ absorption diagrams (diagrams 1g and 1h) in addition to the $2N_{\text{DW}}$ contributions. The solid curves ($3N_{\text{DW}}$) are the full calculations including the $3N + \text{FSI}$ diagram (diagram 1i).

Figure 2(a) ($W_{pp} = 2160$ MeV) demonstrates the enhancement of the $3N$ diagrams due to on-shell propagation of the first exchanged pion. The data are taken from an earlier Saclay measurement [3] that did not constrain the angle $[\theta_1]_{\text{c.m.}}$, which we recall is measured

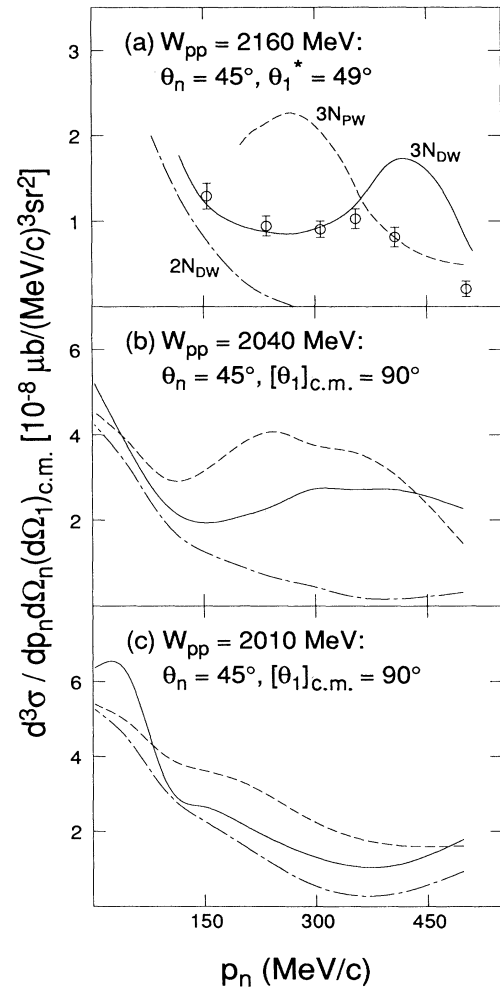


FIG. 2. Reduced cross sections for ${}^3\text{He}(\gamma, pp)n$. The dash-dotted ($2N_{\text{DW}}$) curves include contributions from diagrams 1(a)–1(f), the dashed curves ($3N_{\text{PW}}$) also include diagrams 1(g)–1(h), and the solid line ($3N_{\text{DW}}$) is the full calculation using diagrams 1(a)–1(i). (a) For kinematics above pion threshold where the first exchanged pion travels on-shell; curves and data extracted from Ref. [3]. (b), (c) For the kinematics of the present measurement, where both exchanged pions are off-shell. Fixing $[\theta_1]_{\text{c.m.}} = 90^\circ$ in (b) and (c) reduces the effect of the $3N + \text{FSI}$ diagram [Fig. 1(i)] compared to (a), where $\theta_1^* = 49^\circ$.

w.r.t. the photon beam, but instead fixed the proton angle in the pp c.m. system w.r.t. the direction of the recoiling pp c.m. to be 49° . This angle in Laget's calculations is labeled as θ_1^* . For this case, the contribution from the $3N$ +FSI diagram (1*i*) is significant, and while these data show an enhancement over the $2N_{\text{DW}}$ predictions, they are not well described by either of the $3N$ curves. Furthermore, since the first exchanged pion travels on-shell for these kinematics, the relationship between the $3N$ absorption diagrams and three-body forces is not completely clear.

Our experiment was designed to sample the kinematic regions specified in Figs. 2(b) ($W_{pp} = 2040$ MeV) and 2(c) ($W_{pp} = 2010$ MeV). These kinematics are away from the physically less interesting singularity associated with on-shell pion propagation of the "first" exchanged pion. Both pions are off-shell in the present kinematics, a situation more naturally related to $3N$ forces.

All of the calculations shown in this paper are based on those published in Ref. [6] and use the parametrization of the off-shell NN rescattering amplitudes described in Ref. [10]. The off-shell behavior of the first exchanged pion in diagrams $1g-1i$ at *both* vertices has been included [11] in the calculations shown here with a πN cutoff mass value of $\Lambda_\pi = 1100$ MeV. In addition, the ω -exchange and the pair terms [12] have been included in the $\gamma\pi\pi \rightarrow \pi N$ transition amplitude of the $2N$ absorption diagrams 1*c* and 1*d*. The Laget calculations shown in Fig. 2(a) have already been presented in Ref. [3], and those shown in Fig. 2(b) and 2(c) are presented here for the first time.

III. EXPERIMENT

Coincident proton-proton pairs from the ${}^3\text{He}(\gamma, pp)n$ reaction were measured. A bremsstrahlung photon source was used. A high duty-factor electron beam from the Pulse Stretcher Ring (PSR) at the Saskatchewan Accelerator Laboratory (SAL) was directed on a 0.02 radiation length Al radiator to produce the bremsstrahlung beam. The electron beam was then dumped 90° into a well-shielded Faraday cup located 3 m from the radiator. A schematic overview of the experimental setup is shown in Fig. 3. Electron currents ranging from 1 to $4 \mu\text{A}$ were used, with incident beam energies of 235.0, 264.5, and 266.1 MeV.

The photon beam was collimated to a maximum angle of 4.49 mrad, producing a circular beam 2.3 cm in diameter at the target. After the collimator, a sweep magnet cleared any remaining charged particles from the beam. The photon-beam position was continuously monitored by a beam-profile wire chamber array located downstream from the target. Periodic beam-target alignment was checked with x-ray film exposures. The photon-beam flux was measured with a Wilson-type quantameter [13].

The target system consisted of three high-pressure, room temperature, cylindrical gas cells (7.5 cm diameter, 7.5 cm height) mounted in a remotely controlled vertical ladder. The three cells contained 10 atm of ${}^3\text{He}$, 5 atm of ${}^2\text{H}$, and 3 atm of ${}^1\text{H}$. The ${}^2\text{H}$ and ${}^1\text{H}$ targets were used

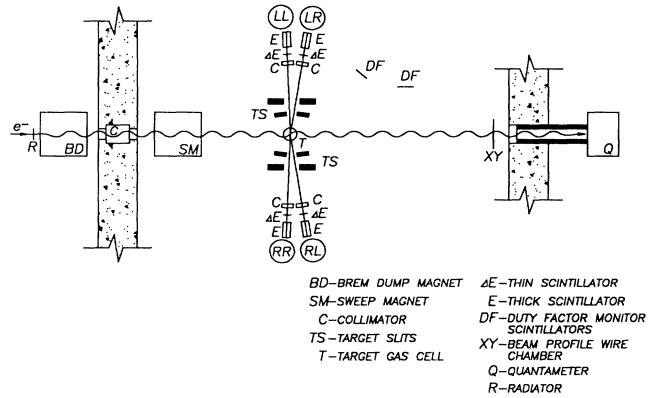


FIG. 3. Schematic overview of the experimental setup (not to scale). Lead shielding surrounding the proton detectors, and placed between the detectors and the front wall, is not shown.

for energy calibration and background subtraction. Slits were employed to shadow the beam entrance and exit regions of the cell wall.

Plastic scintillator (NE102) telescopes with moderate energy resolution were used to detect the protons. As shown in Fig. 3, two telescopes (LL and LR) were positioned at laboratory angles of 91.6° and 81.5° , with respect to the target-pivot point, forming the *left arm*. Telescopes RR and RL were placed at -90.8° and -80.8° respectively and formed the *right arm*. Each telescope consisted of a $10 \text{ cm} \times 10 \text{ cm} \times 3 \text{ mm}$ thick ΔE scintillator and a $16 \text{ cm} \times 16 \text{ cm} \times 36 \text{ cm}$ thick E scintillator. Lead collimators, 8 cm in diameter, in front of each telescope restricted angular acceptances to $\Delta\theta \cong \pm 1.75^\circ$. These defining collimators were located 1.3 m from the target center and subtended solid angles of about 3 msr. Light-emitting diodes (LEDs) were installed on the sides of each E scintillator block and were used to monitor possible gain shifting in the phototubes.

The target slits in front of the detector collimators were surveyed to accurately determine the target length and solid angle subtended by each telescope. The geometric acceptances and central detection angles for each of the four possible *left-arm-right-arm* coincidence combinations are given in Table I. This geometry permitted all four of these coincidence combinations to intercept a portion of the phase space corresponding to Laget's calculations. The values quoted in Table I were generated using a Monte Carlo code to simulate the geometric acceptance [14], defined as the product of tar-

TABLE I. Central detection angles and calculated geometric acceptances.

Detectors	Central angles		Acceptance $t \Delta\Omega_{\text{left}} \Delta\Omega_{\text{right}}$ (cm msr ²)
	θ_{left} (deg)	θ_{right} (deg)	
LR-RL	+81.0	-80.3	34.25
LR-RR	+81.5	-90.8	7.67
LL-RL	+91.7	-80.9	10.51
LL-RR	+92.2	-91.4	33.77

get length and the solid angles. Since the target slits constrain each telescope to view only a portion of the target, central angles and acceptances vary depending on the overlap of the target regions viewed by the left and right telescopes. Thus, the larger acceptances for the *LR-RL* and *LL-RR* combinations reflect the larger common target region compared to the *LR-RR* and *LL-RL* combinations.

Event-mode data acquisition was used to record detector pulse heights and relative timing information for each event. All one-arm events and all two-arm events were recorded. A one-arm event required a twofold coincidence between the ΔE and E scintillators of one telescope. A two-arm event required a fourfold coincidence between a ΔE - E of a left-arm telescope and a ΔE - E of a right-arm telescope. The LEDs on the E blocks were flashed continuously at a rate of 256 Hz. Acquisition was suspended during each LED flash (450 ns), and the E -block pulse heights resulting from every tenth LED flash were recorded for gain monitoring purposes. Typical electronics deadtimes using this trigger mode were 5–10%.

Proton identification was achieved by applying two successive cuts to the data. The first cut defines the proton band appearing on an ΔE vs E scatter plot [Fig. 4(a)]. Similarly, the second cut defines a proton band in a plot of total energy versus the ΔE - E time difference (TDIFF vs E), as shown in Fig. 4(b). Since the first “ ΔE vs E ” cut is quite clean, the effect of the second cut is small. The level of proton identification using these two cuts is greater than 99%. A minimum energy threshold was imposed to reject two-proton events where either proton had a reaction-site energy less than 28.5 MeV, since protons below this energy could not be reliably detected with our system.

Frequent measurements were made using the ^2H and ^1H target cells in order to monitor the gains of the proton detectors, to provide measurements $^2\text{H}(\gamma, p)n$ for checking the normalization of the experimental system, and to serve as (γ, pp) “empty-target” background data.

Energy calibrations of the detectors were determined by fitting the measured $^2\text{H}(\gamma, p)n$ yield to a model bremsstrahlung yield with two known end-point energies, 235 and 266 MeV. One-arm triggers were used in this measurement since the energy and angle of the proton completely determines the reaction kinematics. A minimum pulse-height threshold was imposed to ensure that the final state did not contain a pion. The reaction-site energy was then determined by accounting for the energy loss of the proton between the target and the E block. The model yield folded the “known” $^2\text{H}(\gamma, p)n$ differential cross section with the differential bremsstrahlung cross section. The phenomenological analysis of the world’s $^2\text{H}(\gamma, p)n$ database [15] was used as the “known” deuterium photodisintegration cross section. Calibration constants were determined by fitting the measured yields to the model yields as shown in Fig. 5(a). This yield was corrected for “empty-target” (^1H) background, and the small variations (<10%) in the calibration constants were accounted for by performing fits to every ^2H run (once per 8 hour shift), as well as by monitoring the E -

block LED peak pulse-height positions within runs. Over the range of proton energies relevant to this experiment, a linear relationship between the E -block pulse height and the energy deposited in the block was found to adequately describe the measured yields.

Incident-flux normalization was checked by directly comparing our measured $^2\text{H}(\gamma, p)n$ differential cross sections to the prediction of Ref. [15] [see Fig. 5(b)]. The number of photons incident on the target is determined from the total charge acquired on the quantameter which is proportional to the total energy delivered by the photon beam. The quantameter proportionality constant was well known from previous experiments [16] and our normalizations were found to be accurate to within 10% of the values predicted by Ref. [15].

$^3\text{He}(\gamma, pp)$ events were identified by two-arm trigger events for which a proton was identified in each detector telescope. For every $^3\text{He}(\gamma, pp)n$ event, the angle and en-

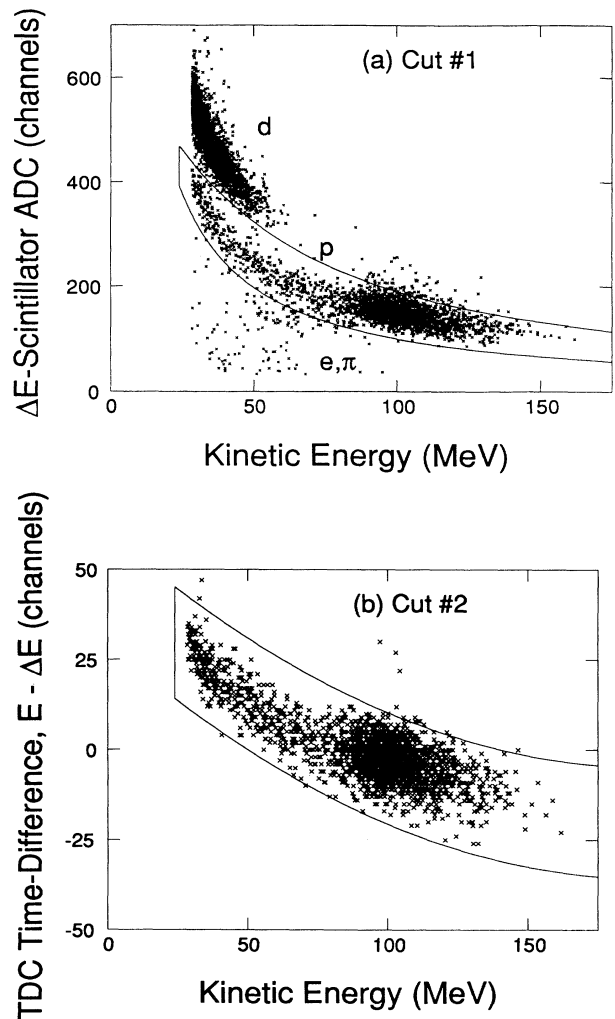


FIG. 4. Method of proton identification for detector *RL* (2-arm trigger data). (a) The position of the E vs ΔE cut applied to all events; (b) the position of the “TDIFF vs E ” cut applied to events surviving the first cut. The TDC setting in *b* is 0.05 ns per channel.

ergy of both protons were measured, completely determining the reaction kinematics. For each electron-beam end-point energy ($E_0 = E_\gamma^{\text{max}}$), a minimum photon-energy threshold ($E_\gamma^{\text{min}} \sim E_0 - 140$ MeV) was imposed to ensure that there was no additional pion in the final state. The ${}^3\text{He}(\gamma, pp)n$ data can be conveniently displayed in either a conventional triangular Dalitz plot or an energy vs energy Dalitz plot (referred to hereafter as a *square* Dalitz plot). A triangular Dalitz plot (Fig. 6) shows the relationship between the center-of-mass kinetic energies of the emitted particles, which are normalized to the available energy, E_{ex} . For nonrelativistic particles of equal mass, the boundary of the triangular Dalitz plot is a circle and, for a given available energy, the three-body phase space is represented by a uniform population of the entire circle [17]. The boundary curve itself corresponds to kinematics in which the three outgoing particle momenta are *collinear* [17].

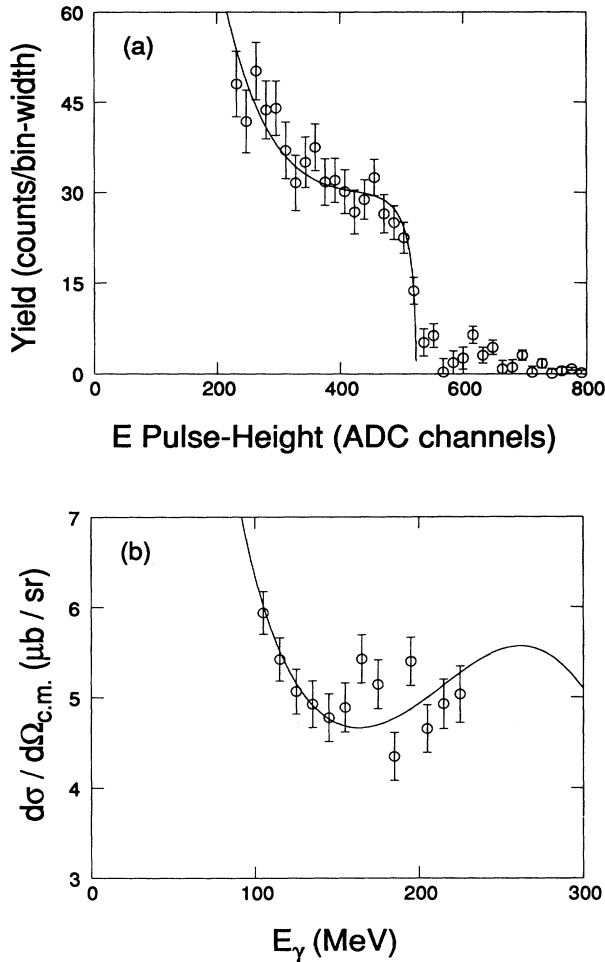


FIG. 5. Sample ${}^2\text{H}(\gamma, p)n$ measurements. (a) Yield for $E_0 = 266$ MeV, detector RR. The line is the model-yield described in the text. The calibration constant relating pulse height to deposited energy was varied to obtain the fit shown. (b) Differential cross sections compared to the prediction of Ref. [14] for detector RL at $E_0 = 235$ MeV.

Since the triangular Dalitz plot makes no reference to particle angles, data from the four left-right detector combinations can be displayed on the same plot. Figure 6 shows all of the ${}^3\text{He}(\gamma, pp)n$ and empty-target data for this experiment. *LR-RL* coincidence events populate the dark band of events along the bottom edge of the boundary circle, *LL-RR* events lie farthest from the edge (closest to the center of the circle), and events from

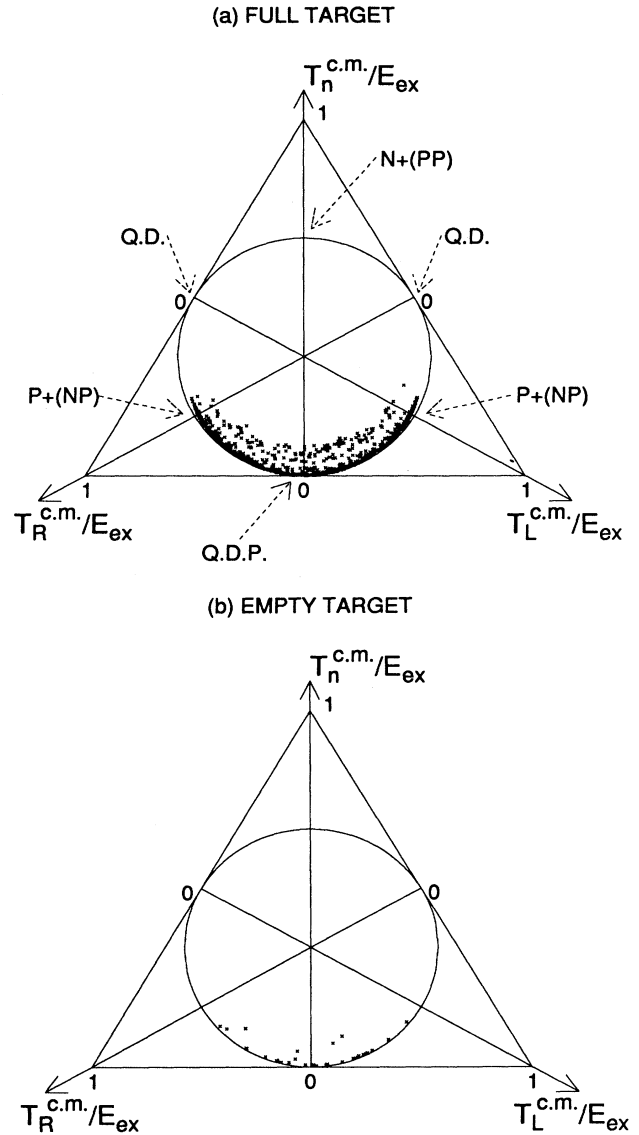


FIG. 6. Triangular Dalitz plots. The three axes are the c.m. kinetic energies for the left proton, right proton, and the neutron, all normalized to the available energy ($E_{\text{ex}} = T_L^{\text{c.m.}} + T_R^{\text{c.m.}} + T_n^{\text{c.m.}}$). The full-target plot contains all the ${}^3\text{He}$ data, and the empty-target plot shows all events obtained using the ${}^2\text{H}$ target. The incident flux for the empty-target runs was 40% of the flux used for the full-target runs. The indicated kinematic regions are the quasidiproton (QDP), quasideuteron (QD), *np*-FSI ($P + NP$), and *pp*-FSI ($N + PP$) regions.

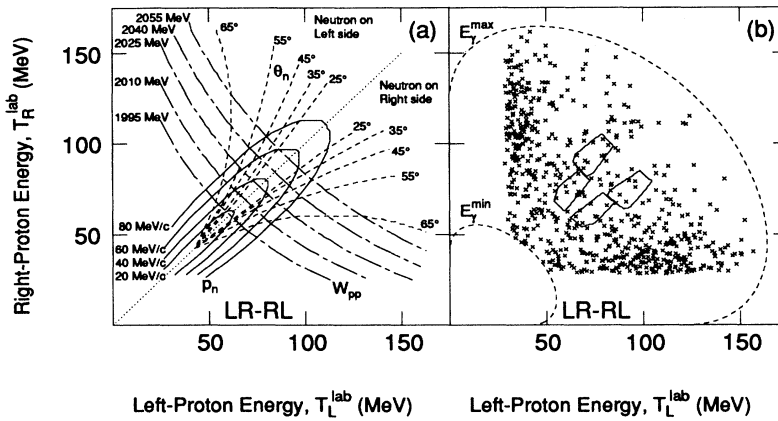


FIG. 7. Square Dalitz plots. (a) Interplay of various kinematic variables for the *LR-RL* detector combination. (b) Regions where cross sections have been extracted, and the measured events, for *LR-RL*. Similar plots can be made for the other three left-right coincidence combinations.

LR-RR and *LL-RL* fall between these other two bands. As a result of our specific detector geometry, the data mainly populate the quasidiproton kinematic region (near $T_n^{c.m.} = 0$). Regions where $2N$ mechanisms should be most important (near $T_L^{c.m.} = 0$ or $T_R^{c.m.} = 0$) remain unpopulated. Note that a small portion of the *LR-RL* events extend up to the “ $P+(NP)$ ” regions. These regions correspond to kinematics in which the neutron and one of the protons are emitted together, with the same vector momentum. It is in these regions that (np) FSI would be expected to be important. The kinematics corresponding to Laget’s calculations are far from these FSI regions.

The accidental-coincidence background requiring a fourfold coincidence (ΔE - E left-arm and ΔE - E right-arm), with both particles identified as protons, was small ($\leq 3\%$) due to the high duty-factor beam. The empty-target background data shown in Fig. 6 are primarily due to target-wall scattering. The empty-target (^1H) background present in the 1-arm-trigger (γ, p) measurements (50–80%) was reduced substantially by imposing the 2-arm-trigger requirement for (γ, pp). The empty-target (γ, pp) background is less than 8% over the entire energy range. Since low statistics prevented the performance of a background subtraction for the (γ, pp) data, this background introduces a systematic uncertainty of (at most) 8% in our (γ, pp) cross sections.

Square Dalitz plots were used to isolate the kinematic regions of interest specified by Laget. For each of the four left-right angular combinations, a square Dalitz plot can be constructed by plotting the kinetic energy of the left proton versus the kinetic energy of the right. Contours for all relevant kinematic variables (e.g., p_n , θ_n , W_{pp}) can be mapped onto a square Dalitz plot for a given

angular combination [see Fig. 7(a)]. Contours for $[\theta_1]_{c.m.}$ are not shown in Fig. 7(a) because $[\theta_1]_{c.m.}$ is nearly determined by the proton angles and depends only minimally on the proton energies: $[\theta_1]_{c.m.} \cong 89^\circ - 91^\circ$ for *LR-RL* and *LL-RR*, and $84^\circ - 85^\circ$ or $94^\circ - 95^\circ$ (depending on which side the neutron is emitted) for *LR-RR* and *LL-RL*.

In order to compare to Laget’s calculations, the data were binned so that the kinematics of each bin center corresponded to the kinematics used in the calculations. The size of the bins about the central values was selected with both statistical and resolution considerations in mind. Ranges of values for bin centers, bin sizes, and detection resolutions for the relevant kinematic variables are given in Table II. Bins were defined as the intersection region of three kinematic variables: ($W_{pp}^{\text{central}} \pm \Delta W_{pp}$), ($\theta_n^{\text{central}} \pm \Delta \theta_n$), and ($p_n^{\text{central}} \pm \Delta p_n$), where “ Δ (variable)” is the bin size from Table II. Once a bin is defined, other variables (e.g., E_γ or $[\theta_1]_{c.m.}$) can be calculated at the bin center. For all bins, $[\theta_1]_{c.m.}$ was in the range $90^\circ \pm 6^\circ$. The bins used for the *LR-RL* combination are shown in Fig. 7(b), where the upper two bins are centered at $W_{pp} = 2040$ MeV and the lower two bins at 2010 MeV. There are two bins for each W_{pp} to account for the neutron being emitted on either the left or right side of the beam. Similar bins were defined for all left-right combinations, giving a total of 11 individual bins for $W_{pp} = 2040$ MeV and 16 bins for 2010 MeV.

The areas containing a heavier concentration of events in Fig. 7(b), along lines of low T_L^{lab} and T_R^{lab} , correspond to the (np) FSI kinematic regions. As can be seen, the bins from which cross sections have been extracted for comparison to Laget’s calculations are not in the regions where these FSI effects are important.

TABLE II. Ranges of values used for bin definitions. The resolution with which θ_n and p_n could be determined varied with energy, and bin sizes for these two variables were chosen to be approximately equal to the detection resolution.

	Kinematic variable		
	W_{pp} (MeV)	θ_n (deg)	p_n (MeV/c)
Bin-center values	2010 or 2040	45 ± 12	40–340
Resolution	$\pm 6 - 8$	$\pm 3 - 15$	$\pm 20 - 30$
Bin size	± 15	$\pm 3 - 15$	$\pm 20 - 30$

IV. RESULTS

Differential cross sections are extracted for each of the defined bins in the kinematic regions-of-interest in the following way:

$$\frac{d^3\sigma_{\text{lab}}}{dp_1 d\Omega_1 d\Omega_2} = \frac{N_{pp}}{\varepsilon_d \rho_{\text{target}}(t\Delta\Omega_1\Delta\Omega_2) \int_{\text{bin}} N_\gamma(E_\gamma) \Delta p_1(E_\gamma) dE_\gamma}, \quad (2)$$

where N_{pp} is the number of events falling within the defined bin, ε_d is the dead-time efficiency factor (typically ~ 0.9), $t\Delta\Omega_1\Delta\Omega_2$ is the geometrical acceptance (see Table I), and ρ_{target} is the ${}^3\text{He}$ target density. This formula arises by subdividing the bin into many bands by cutting along lines of constant photon energy, calculating the differential cross section for each band, and finally averaging over all the bands, weighted by the full acceptance of each band. In this picture, the acceptance for each of the bands is defined as

$$A = \varepsilon_d \rho_{\text{target}}(t\Delta\Omega_1\Delta\Omega_2) N_\gamma \Delta p_1, \quad (3)$$

where N_γ is the number of incident photons in the energy range of the band and Δp_1 is the momentum range of proton "1" intercepted by the band. Reduced cross sections for each bin are obtained by dividing by the kinematic factor, defined in Eq. (1), using the bin center kinematical values. Due to the sparsity of the data, results from the individual bins were grouped into four or five points. These final results are shown in Fig. 8, along with the calculations of Laget. The p_n error bars cover the entire range of p_n values accepted by the individual bins which were grouped together for each data point. Uncertainties in the photon energy were largely determined from uncertainties in the detector energy calibration and limits on its energy resolution and angle definition. Overall these effects are significantly smaller than the above momentum bands and were neglected. The cross section error bars are statistical only.

Cross sections differential in solid angle have also been extracted as a function of photon energy for each of the left-right coincidence combinations. These cross sections utilize all of the acquired data, and are not restricted solely to the kinematic regions specified by Laget. Following the method used in the pion-true-absorption reactions [4], these results are compared to the $3N$ phase-space distribution which arises if the transition matrix element is constant. The extracted experimental cross sections have not used an assumed energy distribution below the minimum threshold of the detectors. Instead,

$$\frac{d^2\sigma}{d\Omega_1 d\Omega_2}(3N) = \frac{(2\pi)^8 \alpha C}{E_\gamma} \int_{p_1^{\text{min}}} \int_{p_2^{\text{min}}} \delta[m_t + E_\gamma - \sqrt{m_n^2 + (q - p_1 - p_2)^2} - E_1 - E_2] p_1^2 p_2^2 dp_1 dp_2. \quad (4)$$

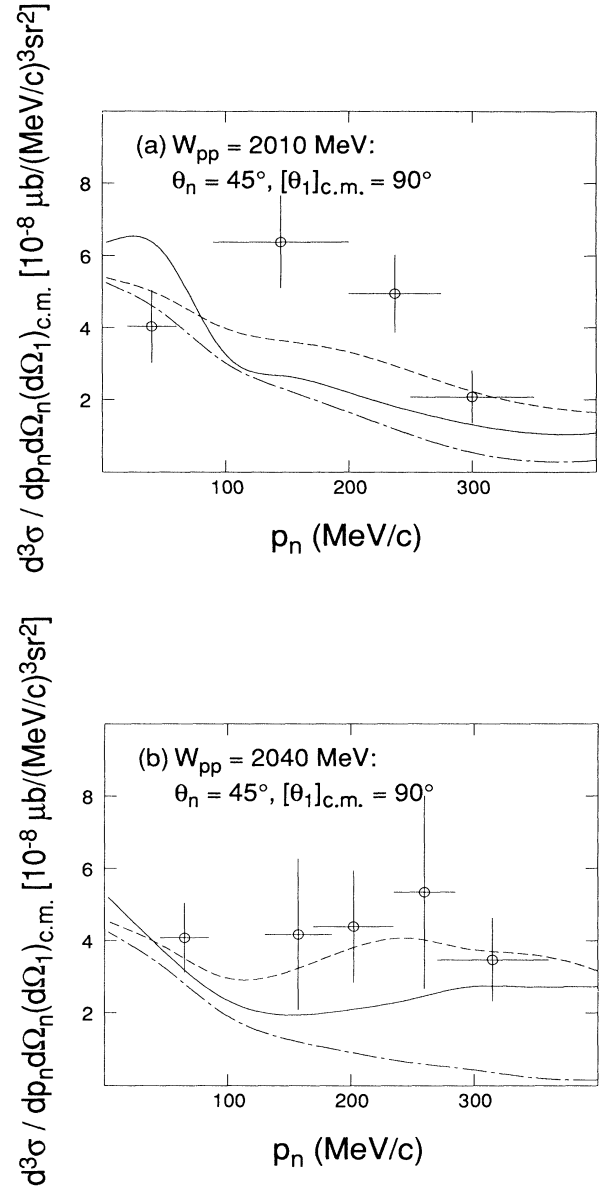


FIG. 8. Results for ${}^3\text{He}(\gamma, pp)n$. Calculations and kinematic constraints are the same as those outlined for Fig. 2.

the quoted results include only integrated cross sections over the proton energies from a minimum kinetic energy of 28.5 MeV ($p_1^{\text{min}} = p_2^{\text{min}} = 233$ MeV/c). The $3N$ phase-space distribution is derived from the general photoabsorption amplitude [18] by fixing the transition matrix element to be constant. The resulting expression used for direct comparison to the experimental results is

The four-momentum of the incident photon is (E_γ, \mathbf{q}) , m_i and m_n are the masses of the ${}^3\text{He}$ target and the neutron. The constant C is determined by a fit to the data and is related to the transition matrix element through

$$C = \frac{1}{2J_i + 1} \sum_{M_i} \sum_{M_f} \frac{1}{2} \sum_{\lambda} |\varepsilon_{\lambda} \mathbf{J}|^2, \quad (5)$$

where \mathbf{J} is the nuclear matrix-element which is averaged over the incident photon polarization (λ) and the initial nuclear spins (M_i), and summed over the final nuclear spins (M_f).

If the measured distributions are consistent with $3N$ phase space, C will be independent of the angular configuration of the detectors. The experimental results and the $3N$ phase-space calculations are shown in Fig. 9, along with the values of C determined for each

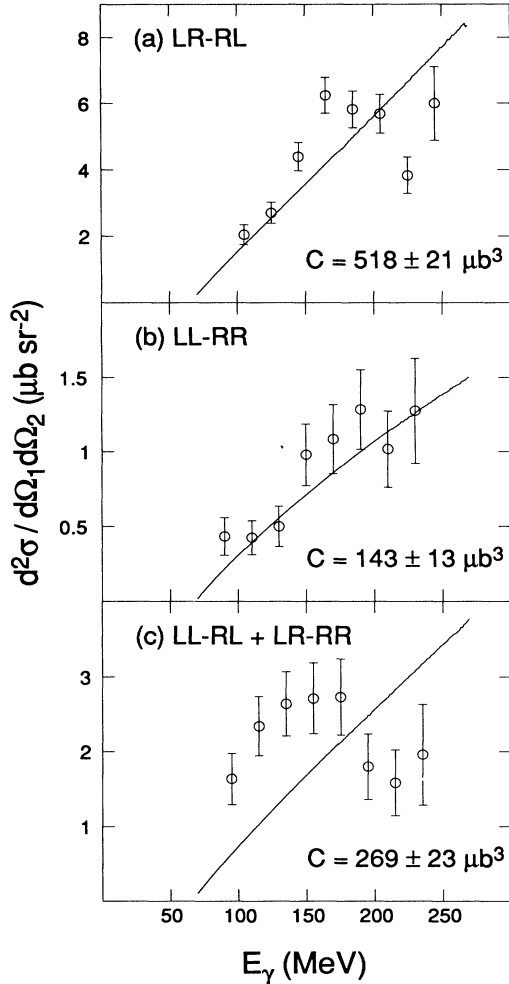


FIG. 9. ${}^3\text{He}(\gamma, pp)n$ cross sections as a function of incident photon energy. The line is a $3N$ phase-space calculation using Eq. (4), and fitted to each data set by varying C . Results for the angular configurations LL - RL and LR - RR have been combined in the bottom graph because of the symmetry of these two configurations. The fitted values for C , and the fit errors, are given for each data set.

configuration. The value of C depends on the angular configuration indicating a non-phase-space angular dependence. Since LR - RL events are mostly collinear in nature, as indicated by the triangular Dalitz plot of Fig. 6, the large value of C for this configuration points to an enhancement of the collinear-geometry cross section as compared to the noncollinear geometries. The shape of the distributions as a function of photon energy follow the trend of the $3N$ phase-space calculation. However, some deviation from the phase-space shape is apparent in all of the angular configurations.

V. SUMMARY

We have measured the differential cross section for the ${}^3\text{He}(\gamma, pp)n$ reaction in phase-space regions where conventional $2N$ absorption mechanisms are minimized, and the relative contribution from a 2π - $3N$ mechanism is expected to be maximized. Our results show an enhancement over the prediction of “ $2N$ only” calculations. This enhancement is most evident at $W_{pp} = 2040$ MeV, where the measurement is 5–9 times greater than the $2N_{\text{DW}}$ prediction for high neutron momenta. The enhancement factor is 3–4 for the 2010 MeV data. The calculations including $3N$ -absorption mechanisms describe the momentum dependence of the data quite well. While our results seem to favor the cross sections predicted by the $3N_{\text{PW}}$ calculation rather than the predictions of the full $3N_{\text{DW}}$ calculation, the $2N_{\text{DW}}$ calculation clearly does not account for the data and the inclusions of a 2π - $3N$ absorption mechanism greatly improves the description of the data. This constitutes direct evidence for the existence of three-body forces in the ${}^3\text{He}$ nucleus, since the 2π -exchange diagram is related to three-body forces when both exchanged pions are off-shell.

Our measurement complements a similar experiment [3] done at higher energies where one of the exchanged pions in the 2π - $3N$ diagram is on-shell. The results of that measurement also show an enhancement over the “ $2N$ only” prediction, but the general shape of that measured neutron distribution was not as clearly described by the inclusion of the 2π - $3N$ mechanism as is our measured distribution. At the higher energies used in Ref. [3], the relationship between the enhancement over $2N$ predictions and nuclear three-body forces is not completely clear since one of the exchanged pions in the 2π diagram is on-shell.

${}^3\text{He}(\gamma, pp)n$ cross sections differential only in the solid angles of the two protons were also measured as a function of photon energy for three angular configurations. The angular and energy dependence of these cross sections were compared to those expected from $3N$ phase-space considerations alone. The measured angular dependence of the cross sections is indicative of a non-phase-space distribution, with an enhancement in the collinear geometry. The measured energy distributions followed the general trend of phase-space predictions, but show a departure from phase space in the range of $E_\gamma \cong 150$ – 200 MeV. These data taken outside of the kinematic region used for comparison with Laget’s calcula-

tions will be useful for further comparison to future realistic calculations.

ACKNOWLEDGMENTS

The authors would like to thank the scientific and technical staff members at SAL, whose hard work and gen-

erous assistance made this experiment possible. We would also like to thank J. M. Laget and E. L. Tomusiak for consulting with us and providing the theoretical help, and the University of Regina REGIE Group for assisting during the initial phase of the experiment. This work was supported by the Natural Sciences and Engineering Council of Canada (NSERC).

-
- [1] C. R. Chen, G. L. Payne, J. L. Friar, and B. F. Gibson, *Phys. Rev. C* **33**, 1740 (1986).
 - [2] G. Audit *et al.*, *Phys. Lett. B* **227**, 331 (1989).
 - [3] G. Audit *et al.*, *Phys. Rev. C* **44**, R575 (1991).
 - [4] K. A. Aniol *et al.*, *Phys. Rev. C* **33**, 1714 (1986); G. Backenstoss *et al.*, *Phys. Lett. B* **222**, 7 (1989); L. C. Smith *et al.*, *Phys. Rev. C* **40**, 1347 (1989); P. Weber *et al.*, *Nucl. Phys. A* **534**, 541 (1991); S. Mukhopadhyay *et al.*, *Phys. Rev. C* **43**, 957 (1991).
 - [5] N. R. Kolb, P. N. Dezendorf, M. K. Brussel, B. B. Ritchie, and J. H. Smith, *Phys. Rev. C* **44**, 37 (1991); N. d'Hose *et al.*, *Phys. Rev. Lett.* **63**, 856 (1989).
 - [6] J. M. Laget, *J. Phys. G* **14**, 1445 (1988).
 - [7] J. M. Laget, *Nucl. Phys. A* **497**, 391 (1989).
 - [8] J. M. Laget, *Phys. Rep.* **69**, 1 (1981).
 - [9] J. M. Laget, *Nucl. Phys. A* **446**, 489c (1985).
 - [10] J. M. Laget, *Phys. Rev. C* **35**, 832 (1987).
 - [11] J. M. Laget, private communication.
 - [12] I. Blomqvist and J. M. Laget, *Nucl. Phys. A* **280**, 405 (1977).
 - [13] R. R. Wilson, *Nucl. Instrum.* **1**, 101 (1957).
 - [14] A. J. Sarty, Ph.D. thesis, University of Saskatchewan, 1992 (unpublished).
 - [15] P. Rossi *et al.*, *Phys. Rev. C* **40**, 2412 (1989).
 - [16] D. Delli Carpini *et al.*, *Phys. Rev. C* **43**, 1525 (1991); E. J. Austin *et al.*, *Phys. Rev. Lett.* **61**, 1525 (1988).
 - [17] R. Hagedorn, *Relativistic Kinematics* (Benjamin, New York, 1963).
 - [18] T. de Forest, Jr. and J. D. Walecka, *Adv. Phys.* **15**, 1 (1966).